



# Sentinel-1 observations of the 2016 Menyuan earthquake: A buried reverse event linked to the left-lateral Haiyuan fault



H. Wang<sup>a,b,c,\*</sup>, J. Liu-Zeng<sup>a</sup>, A.H.-M. Ng<sup>c,d</sup>, L. Ge<sup>d</sup>, F. Javed<sup>e,f</sup>, F. Long<sup>g</sup>, A. Aoudia<sup>e</sup>, J. Feng<sup>h</sup>, Z. Shao<sup>i</sup>

<sup>a</sup> State Key Laboratory of Earthquake Dynamics, Institute of Geology, China Earthquake Administration, Beijing, China

<sup>b</sup> Collaborative Innovation Center of Geospatial Technology, Wuhan University, Wuhan, China

<sup>c</sup> Department of Surveying Engineering, Guangdong University of Technology, Guangzhou, China

<sup>d</sup> School of Civil & Environmental Engineering, The University of New South Wales, Sydney, Australia

<sup>e</sup> The Abdus Salam International Centre for Theoretical Physics, Earth System Physics Section, Trieste, Italy

<sup>f</sup> Centre for Earthquake Studies, National Centre for Physics, Islamabad, Pakistan

<sup>g</sup> Earthquake Administration of Sichuan Province, Chengdu, China

<sup>h</sup> Earthquake Administration of Gansu Province, Lanzhou, China

<sup>i</sup> Institute of Earthquake Science, China Earthquake Administration, Beijing, China

## ARTICLE INFO

### Keywords:

InSAR  
Sentinel-1  
Menyuan earthquake  
Haiyuan fault  
Fault interaction  
Geometric complexity

## ABSTRACT

Knowledge on the interaction of active structures is essential to understand mechanics of continental deformation and estimate the earthquake potential in complex tectonic settings. Here we use Sentinel-1A radar imagery to investigate coseismic deformation associated with the 2016 Menyuan (Qinghai) earthquake, which occurred in the vicinity of the left-lateral Haiyuan fault. The ascending and descending interferograms indicate thrust-dominated slip, with the maximum line-of-sight displacements of 58 and 68 mm, respectively. The InSAR observations fit well with the uniform-slip dislocation models except for a larger slip-to-width ratio than that predicted by the empirical scaling law. We suggest that geometric complexities near the Leng Long Ling restraining bend confine rupture propagation, resulting in high slip occurred within a small area and much higher stress drop than global estimates. Although InSAR observations cannot distinguish the primary plane, we prefer the west-dipping solution considering aftershocks distribution and the general tectonic context. Both InSAR modelling and aftershock locations indicate that the rupture plane linked to the Haiyuan fault at 10 km depth, a typical seismogenic depth in Tibet. We suggest that the earthquake more likely occurred on a secondary branch at a restraining bend of the Haiyuan fault, even though we cannot completely rule out the possibility of it being on a splay of the North Qilian Shan thrusts.

## 1. Introduction

The northeastern margin of the Tibetan Plateau accommodates the convergence associated with India-Asia collision according to a combination of fold-thrust belts and strike-slip faults (Tapponnier and Molnar, 1977; Tapponnier et al., 2001) (Fig. 1). The style of deformation varies from west to east in the region. In the west, the convergence is mainly absorbed by the broadly-distributed NW-SE-trending thrust faults with a shortening rate of ~5 mm/yr measured by GPS (Zhang et al., 2004). While in the east, strain is partitioned between the left-lateral strike-slip Haiyuan fault and the North Qilian Shan thrusts in the north (Gaudemer et al., 1995; Lasserre et al., 2002; Liu-Zeng et al., 2007; Daout et al., 2016a). Based on a simplified geological balanced

cross-section Gaudemer et al. (1995), inferred that the Qilian Shan thrusts root on to a south-dipping décollement, which merges with the Haiyuan fault at a depth of ~25 km. Understanding the interaction and deformation partitioning on the thrust and strike-slip faults is essential to estimate the earthquake potential.

The ~1000-km-long Haiyuan fault is the major structure responsible for the eastward movement of Tibet relative to the Gobi-Alashan platform. Its slip rate is still controversial and perhaps spatial-variable from 4 to 8 mm/yr (e.g. Zhang et al., 1988; Li et al., 2009; Duvall and Clark, 2010; Chen et al., 2014; Jolivet et al., 2012; Daout et al., 2016a) to larger than 10 mm/yr (e.g. Gaudemer et al., 1995; Lasserre et al., 1999, 2002). The region around the Haiyuan fault system is one of the most seismically active areas in Tibet with many devastating earth-

\* Corresponding author at: Department of Surveying Engineering, Guangdong University of Technology, Guangzhou, China.  
E-mail address: [ehwang@163.com](mailto:ehwang@163.com) (H. Wang).

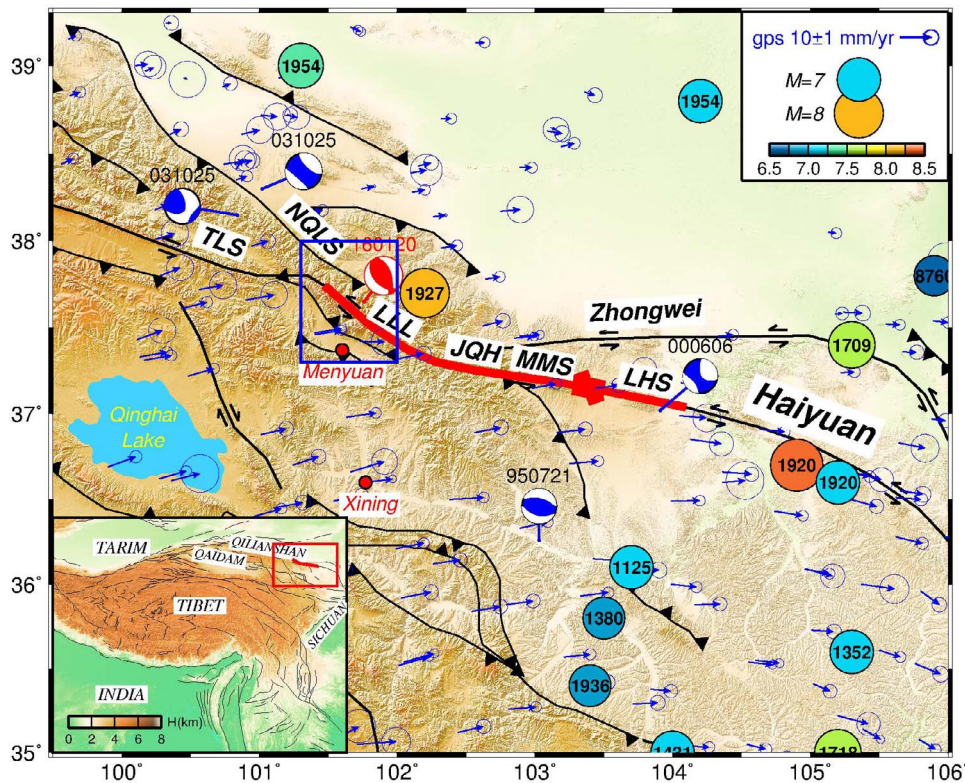


**Fig. 1.** Tectonic map and historical earthquakes around the Haiyuan fault. The coloured circles with year of occurrence inside denote  $M \geq 6.5$  historical earthquakes until 1990 from Gu (1983) and the GCMT catalogue. The blue-white “beach-balls” with dates (yymmdd) on top represent focal mechanisms of the earthquakes since 1991. The 2016 Menyuan earthquake is as a red-white “beach-ball”. The active faults are from Taylor and Yin (2009), in which the Tianzu seismic gap is highlighted with a thick red line. The blue box delimits the extents of the interferograms shown in Fig. 2. Abbreviations of the fault names are NQLS – North Qilian Shan, TLS – Tuo Lai Shan, LLL – Leng Long Ling, JQH – Jin Qiang He, MMS – Mao Mao Shan, LHS – Lao Hu Shan. Blue arrows are GPS velocities from Liang et al. (2013). Inset is the topography and active faults in the whole Tibetan Plateau. The red box indicates the location of the major figure, and the red line highlights the Tianzu gap. (For interpretation of the references to color in this figure legend, the reader is referred to the web version of the article.)

quakes, such as the 14 October 1709  $M_w$  7.5 Zhongwei, the 16 December 1920  $M_w$  7.8 Haiyuan and the 22 May 1927  $M_w$  7.9 Gulang events (Gu, 1983; Deng et al., 1986; Liu-Zeng et al., 2007). In which, the 1920 earthquake caused severe casualties killing at least 220,000 people (Liu et al., 2003). Between the Haiyuan and Gulang earthquakes, the ~260-km-long segment has been absent of large earthquake over 800 years. It was therefore considered as a seismic gap, namely “Tianzu gap”, where may generate  $M \geq 7.5$  earthquakes (Gaudemer et al., 1995). The Tianzu gap is composed of four segments from east to west including Lao Hu Shan, Mao Mao Shan, Jin Qiang He and Leng Long Ling (LLL) (Gaudemer et al., 1995).

On 20 January 2016, a  $M_w$  5.9 earthquake occurred in Menyuan county, about 55 km west of the 1927 Gulang earthquake and 110 km north of Xining – the provincial capital of Qinghai. It is the largest since the 26 August 1986  $M_w$  5.9 earthquake. The epicentre lies between the east end of the North Qilian Shan fault and the west end of the Tianzu gap near the LLL mountain (Fig. 1). The south flank of the LLL mountain range is bounded by north-dipping reverse faults and thus separated from the Tertiary Menyuan basin. Together, the fault system near the Menyuan earthquake resembles a crustal-scale flower-structure. Geometric complexities here might affect the initiation and propagation of the Menyuan earthquake ruptures (King and Nabelek,

1985; Wesnousky, 2006). It is also not clear whether this earthquake signals an increase loading on the Haiyuan fault, or it is an aftershock of the 1927 Gulang earthquake. Its mechanism and structural affinity therefore should shed light on understanding the interaction of active structures and clarifying which fault the earthquake is associated. Although reverse events are common in northeastern Tibet, none of them has been investigated using geodesy except for the 2008/2009 Qaidam earthquakes whilst far from the Haiyuan fault (Elliott et al., 2011). This enhances the importance of the Menyuan earthquake for studying regional tectonics and seismic potential, given that it occurred roughly near the end of the seismic gap. Using Sentinel-1A data, Li et al. (2016) derived coseismic deformation and a dislocation model of the Menyuan earthquake. Here we provide different solutions from similar radar imagery together with aftershock relocation and Coulomb stress changes.

## 2. InSAR data analysis

We use two pairs of Sentinel-1A radar images acquired in TOPS mode on the ascending track 128 and descending track 033, respectively. These datasets have the shortest temporal and perpendicular baselines available (Table 1). We produce interferograms from the SLC

**Table 1**  
Interferometric pairs used in this study.

Master-slave (yymmdd)	Orbit direction	Track	$B_{\perp}$ (m)	$B_T$ (day)	Incidence (degree)	$\sigma$ (mm)	$\alpha$ (km)
160113–160206	Ascending	128	17	24	36–40	5	19
160118–160211	Descending	033	12	24	34–38	3	13

products using the GMT5SAR software developed at UCSD (Sandwell et al., 2016). The along-track doppler centroid variation of TOPS mode makes the azimuth coregistration more difficult than the conventional strip-map processing. Coregistration accuracy of at least 0.001 pixel is necessary to eliminate this effect (Zan and Gurarnieri, 2006). To overcome this issue, we conduct three steps including geometric alignment based on precise orbits (Sansosti et al., 2006), deramping of SLC data prior to interpolation (Miranda, 2015), and overall correction of mis-registration errors based on enhanced spectral diversity (Prats-Iraola et al., 2012). Detailed implementations can be found in the manual of GMT5SAR (Sandwell et al., 2016). Topographic phase is removed using a 1-arc-second SRTM DEM (Farr et al., 2007). The interferograms are smoothed with a power spectrum filter (Goldstein and Werner, 1998) and then unwrapped using the SNAPHU software (Chen, 2001). Each sub-swath of the interferometric pair is processed independently in radar coordinates. They are finally assembled in geographic coordinates based on the average differences of two neighbouring swaths at the overlapping area. The smooth fringes imply that burst mis-alignment, the most challenging problem aforementioned for TOPS imagery, has been well sorted out (Fig. S1).

We estimate orbital and atmospheric delay errors in InSAR observations while masking the epicentral area as indicated in Fig. S1. The orbital errors are modelled using a bi-linear function. The atmospheric delay errors are quite strong due to significant elevation changes in the mountain region. We fit such artefacts using a linear function between InSAR observations and heights. The resultant interferograms show

clear surface deformation on top of the LLL segment (Fig. 2). The continuous NW-SE-oriented elliptical fringes imply a buried event roughly striking parallel to the LLL segment. Both ascending and descending data show major motion towards the satellite, with the maximum displacements of about 58 and 68 mm respectively. For line-of-sight (LOS) projection, eastward motion can cancel part of uplift in ascending geometry while strengthen in descending. Therefore, larger descending displacements indicate eastward motion of the hanging wall, corresponding to either left-lateral slip for a west-dipping or right-lateral slip for an east-dipping fault plane.

### 3. InSAR modelling

We use a quadtree algorithm to down-sample the interferograms (Jónsson et al., 2002), resulting in 342 and 402 data points for the ascending and descending pairs respectively. Despite dramatic reduction in quantity, our down-sampled observations well retain the major features of the original interferograms (Fig. S2). The observations are weighted based on a 1-D covariance function  $c_{jk} = \sigma^2 e^{-d_{jk}/\alpha}$  estimated with far-field data (Parsons et al., 2006), where  $c_{jk}$  and  $d_{jk}$  are the covariance and distance between pixels  $j$  and  $k$ ,  $\sigma$  and  $\alpha$  represent standard deviation and e-folding wavelength (Table 1 for their estimates).

We determine source parameters using a rectangular dislocation model in a homogeneous elastic half-space (Okada, 1985), with a shear modulus of 32.3 GPa and a Poisson ratio of 0.25 as in Elliott et al.

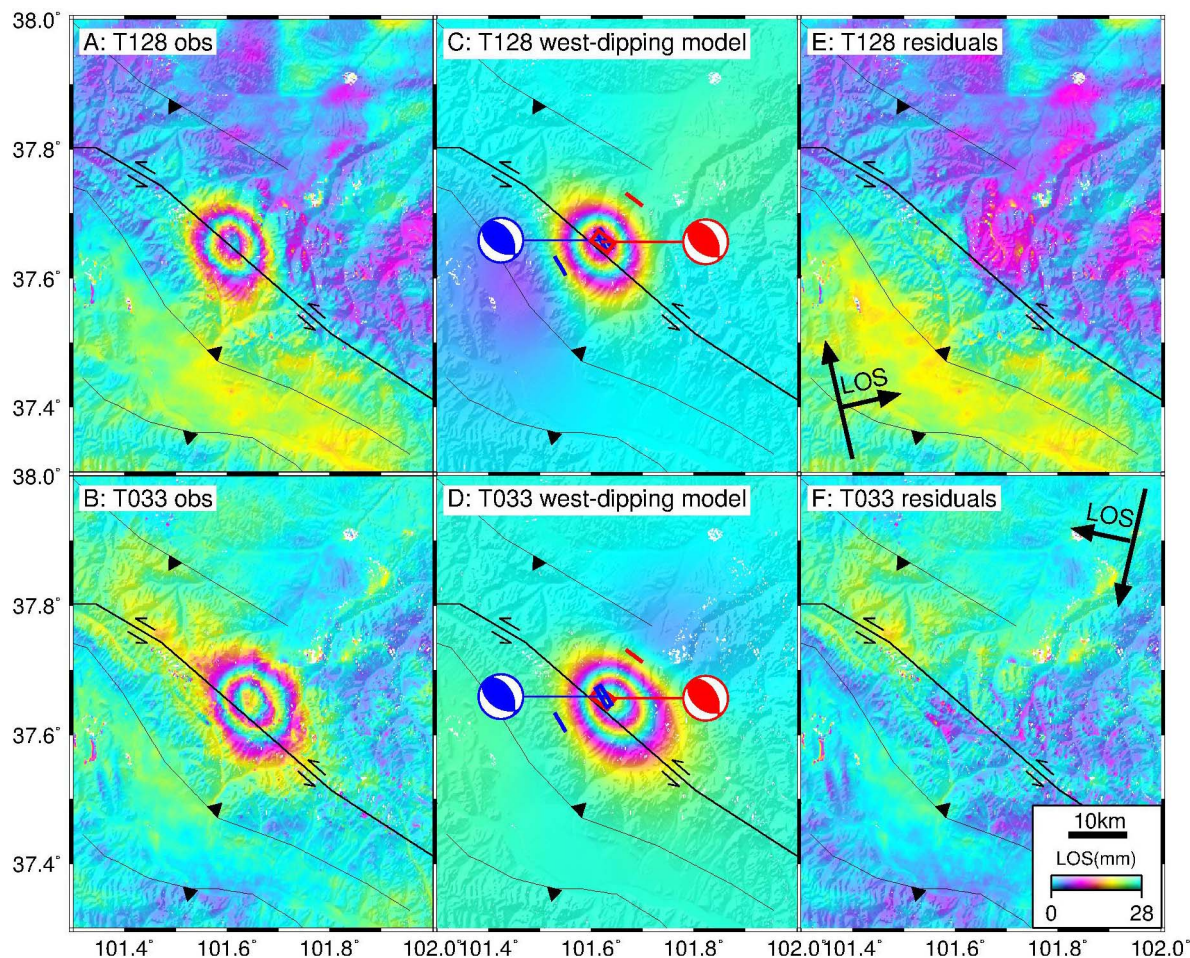


Fig. 2. (a–b) Observations, (c–d) synthetic interferograms and (e–f) residuals from the west-dipping distributed-slip model on the ascending track 128 and descending track 033, respectively. Positive values indicate motion away from the satellite. The red and blue boxes show the surface projections of the west- and east-dipping uniform-slip fault planes respectively, with solid lines representing the fault trace and beach-balls for the focal mechanisms. The short and long arrows indicate radar looking and flight directions. (For interpretation of the references to color in this figure legend, the reader is referred to the web version of the article.)

**Table 2**  
West-dipping (ICMT-W) and east-dipping (ICMT-E) fault parameters and 1-sigma uncertainties from InSAR, and as listed in the USGS catalogue.

Model	Longitude (°)	Latitude (°)	Depth (km)	Strike (°)	Dip (°)	Rake (°)	Length (km)	Width (km)	Slip (m)	$M_0$ ( $10^{17}$ Nm)	$M_w$
USGS	101.641	37.671	9	134/343	43/51	68/109				9.912	5.967
ICMT-W	101.623	37.657	9	127	45	73	3.5	3.0	2.256	7.612	5.891
	± 0.003	± 0.002	± 0.2	± 6	± 2	± 5.6	± 0.9	± 1.1	± 0.5	± 0.4	± 0.015
ICMT-E	101.625	37.659	9	329	46	109	3.7	1.4	4.555	7.571	5.889
	± 0.002	± 0.002	± 0.2	± 5	± 2	± 4.3	± 0.8	± 0.3	± 0.4	± 0.4	± 0.014

(2011). Since orbital and atmospheric delay errors have been removed with far-field data, here we just consider two constant offsets to unify the reference of ascending and descending data. The uncertainties and trade-offs of model parameters are evaluated using a Monte-Carlo analysis (Wright et al., 1999). In this method, we generate 100 sets of spatially correlated random noise, a typical number used in many studies (e.g. Wright et al., 1999; Elliott et al., 2010), based on the 1-D covariance function. The observations are then perturbed by adding the simulated noise. We constrain a solution for each of the perturbed data set, and used the 100 solutions to estimate errors and trade-offs between parameters.

For uniform-slip modelling, we use a hybrid simulated annealing and quasi-Newton algorithm to find the best-fit models (Cervelli et al., 2001; Jónsson et al., 2002). We set a priori bounds after trial-and-error tests to improve the efficiency of non-linear inversion, and manually adjust if the solutions converged to the upper or lower bounds. The final lower and upper bounds of the source parameters are given in Table S1. Table 2 lists the source parameters and their 1-sigma uncertainties (named as ICMT, i.e. InSAR CMT), as well as the USGS solution. Figs. S3 and S4 show distributions of the source parameters for a west- and east-dipping fault plane, respectively. Li et al. (2016) regarded a secondary LLL fault as responsible for the earthquake, therefore assumed the fault plane dipping to the southwest and fixed the top edge as the geological surface trace in their preferred two-segment model. Here we find coseismic deformation can be fit quite well using a single-segment fault without any assumption of fault location and orientation (Figs. S5 and S6). Both west- and east-dipping models give root-mean-square errors (RMSE) of about 5.4 and 3.4 mm for the ascending and descending data respectively, comparable to their a-priori uncertainties in the covariance functions. So the primary nodal plane is not able to be determined according to a smaller RMSE. Regardless of which nodal plane is the primary, our estimates of strike, dip and rake agree very well with the USGS double-couple solutions. Our estimates of centroid depth are 9 km for both nodal planes, almost identical to the manually revised USGS solution but 1.5 km shallower than that in Li et al. (2016). The difference of the horizontal centroid locations is about 2 km between the USGS and our solutions.

In order to get more physically reasonable solution, we invert slip distribution for both nodal planes while fixing the reference offsets, centroid location, strike and dip from the uniform-slip models. We solve strike- and dip-slip distribution using a bounded variable least-squares method (Stark and Parker, 1995; Wang et al., 2007), with a Laplacian operator to ensure reasonable solutions. The Laplacian smoothing factor is selected according to a trade-off curve between weighted misfit and solution roughness (Fig. 3a). Despite smaller width in the east-dipping uniform-slip model, the slip distribution for both nodal planes has similar elliptical pattern, with shallower slip towards northwest (Figs. 3 and S7). The difference of their residuals is no more than 3 mm, within 1-sigma errors of the observations (Figs. 2 and S8). The resultant scalar moments are  $9.927 \times 10^{17}$  Nm ( $M_w$  5.968) and  $9.907 \times 10^{17}$  Nm ( $M_w$  5.967) respectively, consistent with the USGS solution but slightly larger than that from the uniform-slip models. Our solutions show that most slip focuses around the origin of the earthquake, about 66% occurred within an area of about  $8 \times 6$  km and the maximum is about 0.75 m. Li et al. (2016) suggested the earthquake

was nucleated at deeper portion and propagated upwards based on their shallower slip distribution than the centroid depth. This might be due to their imperfect constraints on the centroid depth and fault size, for example, it is unlikely that the fault size of  $20 \times 10$  km assumed in their uniform-slip model is even larger than the range of slip distribution.

## 4. Discussion

### 4.1. Geometric complexity and fault rupture size

Geometric complexities such as fault bends, branches and step-overs are ubiquitous along strike-slip faults, such as the transcompressional bend of the San Andreas Fault (Yule and Sieh, 2003) and the North Anatolian Fault around the Sea of Marmara (Barka and Kadinsky-Cade, 1988). They are considered to affect the initiation and propagation of earthquake ruptures, and can control the ultimate size of earthquakes (King and Nabelek, 1985; Wesnousky, 2006). The strike of the Haiyuan fault near Menyuan changes from about  $100^\circ$  at JQH to  $125^\circ$  at LLL and back to  $100^\circ$  again at TLS within a distance of about 100 km, forming a “Big Bend” of the Haiyuan fault (Fig. 1). According to the scaling law (Wells and Coppersmith, 1994), the predicted rupture length and width are about 10.5 and 6.6 km respectively for a magnitude of 5.9 earthquake. Our uniform-slip modelling can exclude a possible nodal plane with such size (Figs. S3 and S4) or even almost twice in Li et al. (2016). The distributed-slip models also show that most slip focused within a small area. We estimate the stress drop of about 20 MPa on a rectangular dip-slip fault (Stein and Wysession, 2003), much higher than the global median of 2–3 MPa for reverse and 6 MPa for intraplate earthquakes (Allmann and Shearer, 2009). The well-constrained focal location indicates that the earthquake occurred between the North Qilian Shan thrusts and the bending LLL segment of the Haiyuan fault. Such a complex context may confine rupture propagation, thus yielding high slip and stress drop on a small fault plane.

### 4.2. Dip orientation

Since both nodal planes give approximately equal misfits, it is always challenging from geodetic data to determine dip orientation for a buried reverse earthquake at small or moderate size (Lohman et al., 2002; Lohman and Barnhart, 2010). Other information is then required such as the empirical scaling law of source parameters, aftershocks and tectonic context. Some studies ruled out an orientation that has an extremely large slip-to-width ratio in terms of the scaling law (Wang et al., 2014). However, both nodal planes here have relatively larger slip-to-width ratio than that expected for a  $M_w$  5.9 earthquake according to the empirical relationship in Wells and Coppersmith (1994). Considering the strong trade-off between width and slip, slight changes of width can cause significant changes of slip for a narrow fault. Our synthetic data give uniform distribution of dip-slip within the pre-defined search bounds (Fig. S4), implying that the even larger slip-to-width ratio in the east-dipping model is due to poorer constraints on slip. Both models give similar slip distribution patterns, reinforcing the incapability of distinguishing dip orientation in terms of the scaling law.

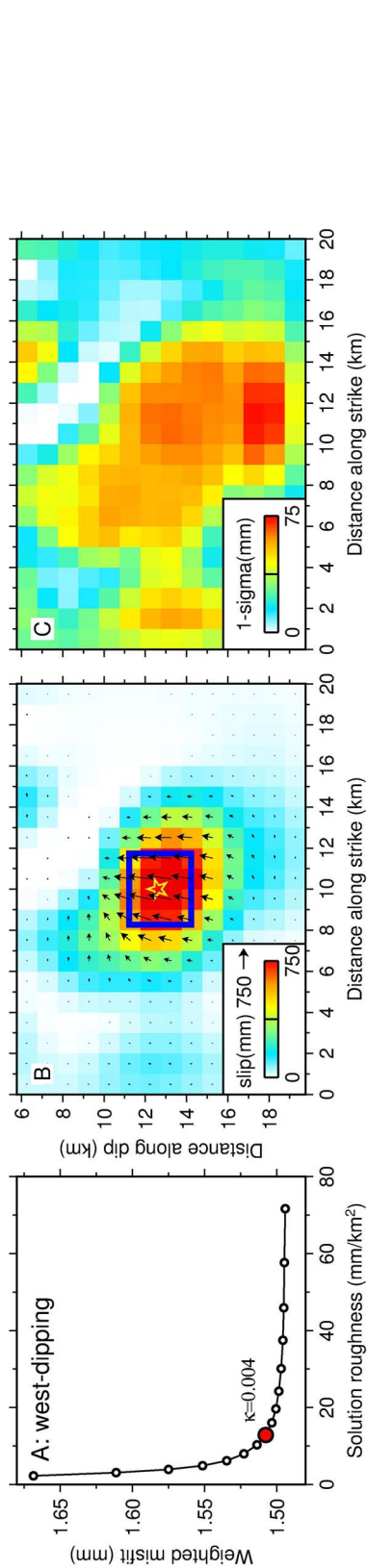


Fig. 3. (a) Trade-off curve between weighted misfit and solution roughness for a west-dipping nodal plane. The red dots denote the optimal smoothing factor of 0.004 used to generate, (b) slip distribution and (c) the associated 1-sigma errors. Arrows indicate slip directions on the hanging wall, viewing along strike. The star and blue box indicate the origin and the area of the uniform-slip fault model, respectively. (For interpretation of the references to color in this figure legend, the reader is referred to the web version of the article.)

We collect broadband records from 38 local stations in Gansu and Qinghai provinces with an average aperture of about 50 km. The nearly hyperbolic shape of the histogram indicates that the aftershock decay generally obeys the Omori law (Fig. 4a). Following Long et al. (2015), we relocate the aftershocks using a hybrid approach adapted from the absolute location program HYPOINVERSE-2000 (Klein, 1989) and the double-difference algorithm (Waldhauser and Ellsworth, 2000) (Fig. 4). The 1-sigma errors of our resultant aftershocks are about 0.8, 0.7 and 1.8 km in the east, north and up directions, respectively. The cross section of aftershocks along PP' underneath the fault plane shows west-dipping trend although with smaller dip angle (blue dots in Fig. 4c).

The east-dipping model requires a significant component of right-lateral slip, contrast to the sense of slip in the Haiyuan fault system. In addition, both possible fault planes are located at the eastern side of the Haiyuan fault (Fig. 2), the east-dipping model therefore requires truncating the Haiyuan fault at its seismogenic depth. As a result, the interaction of reverse and strike-slip faults will prevent strain accumulation and earthquake nucleation on the Haiyuan fault. It is less compatible with the context that the Haiyuan fault is the leading structure in the region which has generated many large earthquakes. As a conclusion we prefer the west-dipping model because it is consistent to the aftershock distribution and the stress field in the tectonic context.

### 4.3. Fault interaction and tectonic implications

The interaction between dip-slip and strike-slip faults in north-eastern Tibet is often a matter with much discussion (Gaudemer et al., 1995; Lasserre et al., 2001; Daout et al., 2016a). Based on frequency-time analysis of the seismological data, Lasserre et al. (2001) obtained similar fault parameters (strike, dip and rake) of the 1995  $M_w$  5.6 Yongdeng earthquake to ours of the Menyuan earthquake, despite it is about 100 km south of the Haiyuan fault (Fig. 1). They suggested that the Yongdeng earthquake occurred on a décollement proposed by Gaudemer et al. (1995), linking at depth the south-dipping Qilian Shan thrusts and the left-lateral Haiyuan fault. Here our west-dipping model shows that the fault plane of the Menyuan earthquake linked directly with the Haiyuan fault at 10 km depth (Fig. 4), a typical seismogenic depth in Tibet (Wright et al., 2013). The aftershocks also delimit clear alignment parallel to the general strike of the Haiyuan fault but almost all are located to its east side (Fig. 4a), reinforcing the link of the two faults at depth.

In order to evaluate the effect on the Haiyuan fault from the Menyuan earthquake, we use the Coulomb 3.3 software (Lin and Stein, 2004) to calculate Coulomb Failure Stress changes ( $\Delta CFS$ ). Fig. 5a shows  $\Delta CFS$  at 10 km depth for a receiver fault with strike  $120 \pm 10^\circ$ , dip  $45 \pm 5^\circ$  and rake  $75 \pm 5^\circ$ . It is clear that most aftershocks correlate very well with increased  $\Delta CFS$ . We further make three cross sections across and along the LLL segment. The aftershocks are in decreased  $\Delta CFS$  region in cross sections  $L_1L_2$  and  $L_5L_6$  (Fig. 5b and d), whereas in increased  $\Delta CFS$  region in cross section  $L_3L_4$  (Fig. 5c). The cross section in Fig. 4c also shows that the aftershocks are clustered deeper than the faulting plane. Therefore the aftershocks beneath the fault plane might occur on another splay of active structure or due to near field uncertainties of  $\Delta CFS$  estimates (Helmstetter and Shaw, 2006; Marson, 2006).  $\Delta CFS$  calculations indicate that the Menyuan mainshock induced stresses and promoted seismic activities on the nearby thrust faults, with 90% aftershocks occurred on the thrust structures and only 10% localised on the LLL segment. The average  $\Delta CFS$  is negative on the LLL segment while it is negligible on the rest of Haiyuan fault, indicating that the Menyuan faulting has partly released the strain accumulated in the LLL segment.

It remains unclear which structure the seismogenic fault of the Menyuan earthquake belongs to. Both mainshock strike and aftershock distribution show clear alignment almost parallel to the Haiyuan fault. The earthquake therefore is unlikely associated with a right-order alignment between the Haiyuan fault and its secondary splay to the

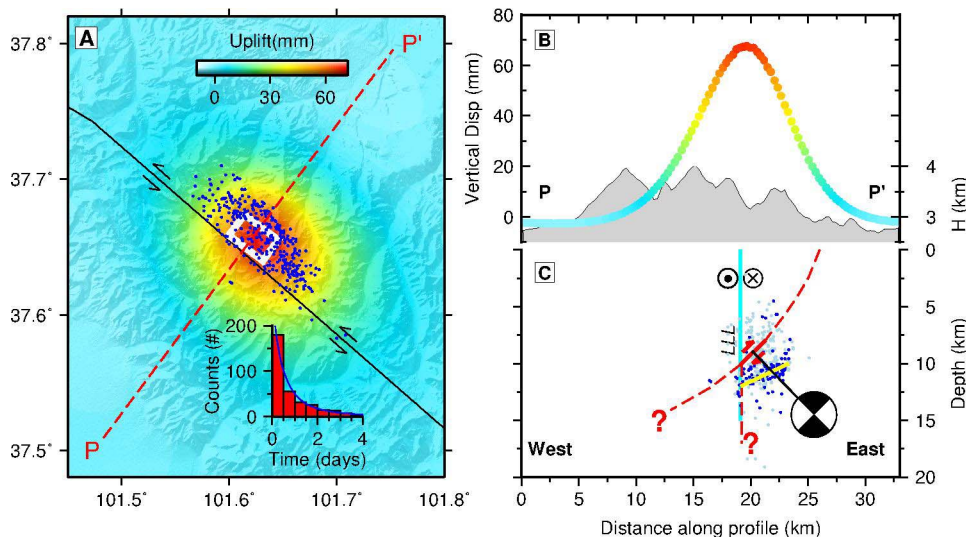


**Fig. 4.** (a) Surface projection of the aftershocks (blue dots) and fault plane (white rectangle) overlain on the vertical displacements derived from the west-dipping distributed-slip model. The inset histogram shows aftershock decay. (b) Vertical displacements along the profile  $PP'$ . (c) Cross-section along the profile  $PP'$  showing interaction of the west-dipping faulting (red) and the LLL segment (cyan). Blue dots denote aftershocks within a swath width as the uniform-slip fault length (i.e., 3.7 km), while the rest are in light colour. The yellow line highlights the orientation of the blue aftershocks. The beach-ball denotes the focal mechanism projected on the fault plane. (For interpretation of the references to color in this figure legend, the reader is referred to the web version of the article.)

north as suggested by Li et al. (2016). We propose two possible interpretations indicated by the dashed lines with question marks in Fig. 4c: (i) an extension of the North Qilian Shan thrusts at depth or (ii) a secondary splay of the Haiyuan fault. It is straightforward to explain the thrust-dominated motion with the former schematic model, which also agrees with the tectonic models at larger scale (Gaudemer et al., 1995). If so, the released normal stress through the Menyuan earthquake might facilitate the initiation of a future large strike-slip event in this seismic gap (King and Nabelek, 1985; Daout et al., 2016). However, these two faults intersect at a typical seismogenic depth, shallower than the expect of a décollement beneath a leading strike-slip structure. So the rupture plane might just represent a splay fault of the North Qilian

Shan thrusts. Alternatively, the main strands of continental strike-slip faults are usually accompanied by secondary contractional and extensional structures where local vertical motion has been commonly observed in the field as well as in theoretical models (Barka and Kadinsky-Cade, 1988; Duvall et al., 2013). The restraining bend around the LLL segment is ideal to enhance strain accumulation that can lead to a thrust-dominated earthquake. In addition, this schematic model also satisfies all the other evidence: (1) left-lateral components of slip, (2) link and alignment to the main strand of the Haiyuan fault, and (3) shallower depth than the expect of a décollement here. Therefore, we think that the seismogenic fault of the Menyuan earthquake is more likely governed by the Haiyuan fault system, and might be merged

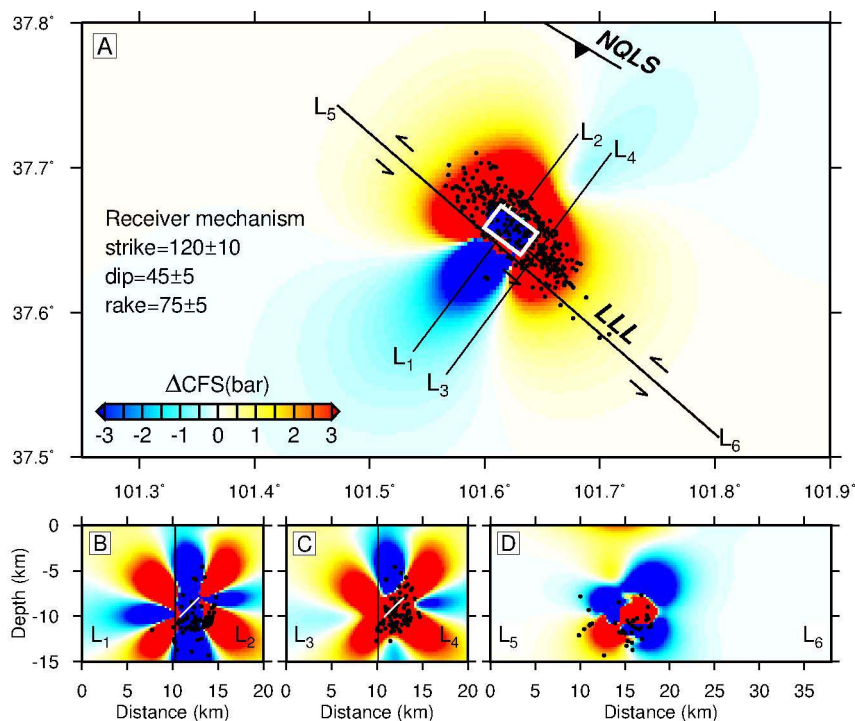


**Fig. 5.**  $\Delta CFS$  caused by the Menyuan earthquake. (a)  $\Delta CFS$  at 10 km depth. The white rectangle shows the rupture area of the mainshock. Black circles denote aftershocks. (b–d)  $\Delta CFS$  on the cross sections  $L_1L_2$ ,  $L_3L_4$  and  $L_5L_6$  which are labeled in Fig. 5a. The black and white lines in Fig. 5b and c mark the location of the LLL segment and the faulting plane, respectively.

together at depth (Fig. 4c), even though we can not completely rule out a splay of the Qilian Shan thrusts.

## 5. Conclusions

We investigate the coseismic deformation associated with the 2016 Menyuan earthquake using Sentinel-1A data. The InSAR observations show thrust-dominated motion as well as apparent strike-slip components, consistent with the tectonic context in northeastern Tibet. We prefer a west-dipping model considering aftershock locations and tectonic context. This model gives a high-angle fault with a dip of 45° striking parallel to the main strand of the Haiyuan fault. Geometric complexities confine the rupture size, resulting in high slip and stress drop occurred on a small fault plane. InSAR modelling and relocated aftershocks show the bottom of the west-dipping fault plane linked to the Haiyuan fault at around 10 km depth. It is still an open question whether the rupture is affiliated with the North Qilian Shan thrusts, or it belongs to a secondary structure of the Haiyuan fault.

## Acknowledgements

The work was supported by the NSFC (41372221, 41672205, 41225010) and the State Key Laboratory of Earthquake Dynamics (LED2013B04). Part of the work was conducted in ICTP through a Regular Associateship awarded to HW. We thank Carolina Pagli for helpful discussion, Charlotte Bishop and an anonymous reviewer for thorough overview and constructive comments. Sentinel-1 data are copyrighted by ESA. We used the GMT5SAR software to produce InSAR data, and the Generic Mapping Tools to prepare the figures.

## Appendix A. Supplementary data

Supplementary data associated with this article can be found, in the online version, at <http://dx.doi.org/10.1016/j.jag.2017.04.011>.

## References

- Allmann, B.P., Shearer, P.M., 2009. Global variations of stress drop for moderate to large earthquakes. *J. Geophys. Res.* 114, B01310. <http://dx.doi.org/10.1029/2008JB005821>.
- Barka, J.A., Kadinsky-Cade, K., 1988. Strike-slip fault geometry in Turkey and its influence on earthquake activity. *Tectonics* 7, 663–684.
- Cervelli, P., Murray, M.H., Segall, P., Aoki, Y., Kato, T., 2001. Estimating source parameters from deformation data, with an application to the March 1997 earthquake swarm off the Izu Peninsula, Japan. *J. Geophys. Res.* 106, 11217–11237.
- Chen, C.W., 2001. Statistical-Cost Network-Flow Approaches to Two-Dimensional Phase Unwrapping for Radar Interferometry. (Ph. D. thesis) Stanford University.
- Chen, T., Zhang, P., Liu, J., Li, C., Ren, Z., Hudnut, K.W., 2014. Quantitative study of tectonic geomorphology along Haiyuan fault based on airborne LiDAR. *Chin. Sci. Bull.* 59, 2396–2409.
- Daout, S., Barbot, S., Peltzer, G., Doin, M.P., Liu, Z., Jolivet, R., 2016. Constraining the kinematics of metropolitan Los Angeles faults with a slip-partitioning model. *Geophys. Res. Lett.* 43, 1192–1201.
- Daout, S., Jolivet, R., Lasserre, C., Doin, M.P., Barbot, S., Tapponnier, P., Peltzer, G., Socquet, A., Sun, J., 2016a. Along-strike variations of the partitioning of convergence across the Haiyuan fault system detected by InSAR. *Geophys. J. Int.* 205, 536–547.
- Deng, Q., Chen, S., Song, F., Zhu, S., Wang, Y., Zhang, W., Jiao, D., Burchfiel, B.C., Molnar, P., Royden, L., Zhang, P., 1986. Variations in the geometry and amount of slip on the Haiyuan (Nanxihaihan) fault zone, China and the surface rupture of the 1920 Haiyuan earthquake. In: Das, S., Boatwright, J., Scholz, C. (Eds.), *Earthquake Source Mechanics*. American Geophysical Union, pp. 169–182.
- Duvall, A.R., Clark, M.K., 2010. Dissipation of fast strike-slip faulting within and beyond northeastern Tibet. *Geology* 38, 223–226.
- Duvall, A.R., Clark, M.K., Kirby, E., Farley, K.A., Craddock, W.H., Li, C., Yuan, D.Y., 2013. Low-temperature thermochronometry along the Kunlun and Haiyuan faults, NE Tibetan plateau: evidence for kinematic change during late-stage orogenesis. *Tectonics* 32, 1190–1211.
- Elliott, J.R., Parsons, B., Jackson, J.A., Shan, X., Sloan, R.A., Walker, R.T., 2011. Depth segmentation of the seismogenic continental crust: the 2008 and 2009 Qaidam earthquakes. *Geophys. Res. Lett.* 38, L06305. <http://dx.doi.org/10.1029/2011GL046897>.
- Elliott, J.R., Walters, R.J., England, P.C., Jackson, J.A., Li, Z., Parsons, B., 2010. Extension on the Tibetan plateau: recent normal faulting measured by InSAR and body wave seismology. *Geophys. J. Int.* 183, 503–535.
- Farr, T.G., Rosen, P.A., Caro, E., Crippen, R., Duren, R., et al., 2007. The shuttle radar topography mission. *Rev. Geophys.* 45, RG2004. <http://dx.doi.org/10.1029/2005RG000183>.
- Gaudemer, Y., Tapponnier, P., Meyer, B., Peltzer, G., Shunmin, G., Zhitai, C., Huang, D., Cifuentes, I., 1995. Partitioning of crustal slip between linked, active faults in the eastern Qilian Shan, and evidence for a major seismic gap, the ‘Tianzhu gap’, on the western Haiyuan Fault, Gansu (China). *Geophys. J. Int.* 120, 599–645.
- Goldstein, R.M., Werner, C.L., 1998. Radar interferogram filtering for geophysical applications. *Geophys. Res. Lett.* 25, 4035–4038.
- Gu, G., 1983. *Catalogue of Chinese Earthquakes, (1831 B.C. – 1969 A.D.)*. Science Publication Press, Beijing (in Chinese).
- Helmstetter, A., Shaw, B.E., 2006. Relation between stress heterogeneity and aftershock rate in the rate-and-state model. *J. Geophys. Res. (Solid Earth)* 111, B07304. <http://dx.doi.org/10.1029/2005JB004077>.
- Jolivet, R., Lasserre, C., Doin, M.P., Guillaso, S., Peltzer, G., Dailu, R., Sun, J., Shen, Z.K., Xu, X., 2012. Shallow creep on the Haiyuan Fault (Gansu, China) revealed by SAR Interferometry. *J. Geophys. Res. (Solid Earth)* 117, B06401. <http://dx.doi.org/10.1029/2011JB008732>.
- Jónsson, S., Zebker, H., Segall, P., et al., 2002. Fault slip distribution of the 1999  $M_w$  7.1 Hector Mine, California, earthquake, estimated from satellite radar and GPS measurements. *Bull. Seismol. Soc. Am.* 92, 1377–1389.
- King, G., Nabelek, J., 1985. Role of fault bends in the initiation and termination of earthquake rupture. *Science* 228, 984–987.
- Klein, F.W., 1989. User's guide to HYPOINVERSE, a program for VAX computers to solve for earthquake locations and magnitudes. Technical Report. U. S. Geological Survey Open-File Report, 89-314.
- Lasserre, C., Bukchin, B., Bernard, P., Tapponnier, P., Gaudemer, Y., Mostinsky, A., Dailu, R., 2001. Source parameters and tectonic origin of the 1996 June 1 Tianzhu ( $M_w = 5.2$ ) and 1995 July 21 Yongden ( $M_w = 5.6$ ) earthquakes near the Haiyuan fault (Gansu, China). *Geophys. J. Int.* 144, 206–220.
- Lasserre, C., Gaudemer, Y., Tapponnier, P., Mériaux, A.S., der Woerd, J.V., Daoyang, Y., Ryerson, F.J., Finkel, R.C., Caffee, M.W., 2002. Fast late Pleistocene slip rate on the Leng Long Ling segment of the Haiyuan fault, Qinghai, China. *J. Geophys. Res.* 107. <http://dx.doi.org/10.1029/2000JB000060>.
- Lasserre, C., Morel, P.H., Gaudemer, Y., Tapponnier, P., Ryerson, F.J., King, G.C.P., Métiévier, F., Kasser, M., Kashgarian, M., Liu, B., Lu, T., Yuan, D., 1999. Postglacial left slip rate and past occurrence of  $M \geq 8$  earthquakes on the Western Haiyuan Fault, Gansu, China. *J. Geophys. Res.: Solid Earth* 104, 17633–17651.
- Li, C., Zhang, P.Z., Yin, J., Min, W., 2009. Late quaternary left-lateral slip rate of the Haiyuan fault, northeastern margin of the Tibetan Plateau. *Tectonics* 28, TC5010. <http://dx.doi.org/10.1029/2008TC002302>.
- Li, Y., Jiang, W., Zhang, J., Luo, Y., 2016. Space geodetic observations and modeling of 2016  $M_w$  5.9 Menyuan earthquake: Implications on seismogenic tectonic motion. *Remote Sens.* 8. <http://dx.doi.org/10.3390/rs8060519>.
- Liang, S., Gan, W., Shen, C., Xiao, G., Liu, J., Chen, W., Ding, X., Zhou, D., 2013. Three-dimensional velocity field of present-day crustal motion of the Tibetan Plateau derived from GPS measurements. *J. Geophys. Res.: Solid Earth* 118, 5722–5732.
- Lin, J., Stein, R.S., 2004. Stress triggering in thrust and subduction earthquakes and stress interaction between the southern San Andreas and nearby thrust and strike-slip faults. *J. Geophys. Res.* 109.
- Liu, B., Zhang, J., Wu, J., Guo, H., 2003. Reevaluating on casualty in the Haiyuan  $M_s$  8.5 earthquake on December 16, 1920. *Earthq. Res. China* 19, 386–399.
- Liu-Zeng, J., Klinger, Y., Xu, X., Lasserre, C., Chen, G., Chen, W., Tapponnier, P., Zhang, B., 2007. Millennial recurrence of large earthquakes on the Haiyuan fault near Songshan, Gansu Province, China. *Bull. Seismol. Soc. Am.* 97, 14–34.
- Lohman, R.B., Barnhart, W.D., 2010. Evaluation of earthquake triggering during the 2005–2008 earthquake sequence on Qeshm Island, Iran. *J. Geophys. Res. (Solid Earth)* 115, B12413. <http://dx.doi.org/10.1029/2010JB007710>.
- Lohman, R.B., Simons, M., Savage, B., 2002. Location and mechanism of the Little Skull Mountain earthquake as constrained by satellite radar interferometry and seismic waveform modeling. *J. Geophys. Res.* 107. <http://dx.doi.org/10.1029/2001B000627>.
- Long, F., Wen, X.Z., Ruan, X., Zhao, M., Yi, G.X., 2015. A more accurate relocation of the 2013  $M_s$  7.0 Lushan, Sichuan, China, earthquake sequence, and the seismogenic structure analysis. *J. Seismol.* 19, 653–665.
- Marson, D., 2006. Can coseismic stress variability suppress seismicity shadows? Insights from a rate-and-state friction model. *J. Geophys. Res. (Solid Earth)* 111, B06305. <http://dx.doi.org/10.1029/2005JB004060>.
- Miranda, N., 2015. Definition of the TOPS SLC deramping function for products generated by the S-1 IPF. Technical Report. European Space Agency, Paris, France.
- Okada, Y., 1985. Surface deformation due to shear and tensile faults in a half-space. *Bull. Seismol. Soc. Am.* 75, 1135–1154.
- Parsons, B., Wright, T., Rowe, P., Andrews, J., Jackson, J., et al., 2006. The 1994 Sefidabeh (Eastern Iran) earthquake revisited: new evidence from satellite radar interferometry and carbonate dating about the growth of an active fold above a blind thrust fault. *Geophys. J. Int.* 164, 202–217.
- Prats-Iraola, P., Scheiber, R., Marotti, L., Wollstadt, S., Reigber, A., 2012. TOPS interferometry with TerraSAR-X. *IEEE T. Geosci. Remote* 50, 2861–2870.
- Sandwell, D., Mellors, R., Tong, X., Xu, X., Wei, M., Wessel, P., 2016. GMTSAR: An InSAR Processing System Based on Generic Mapping Tools (2nd ed.). Technical Report. Scripps Institution of Oceanography, UC San Diego.
- Sansosti, E., Berardino, P., Manunta, M., Serafino, F., Fornaro, G., 2006. Geometrical SAR image registration. *IEEE T. Geosci. Remote* 44, 2861–2870.
- Stark, P.B., Parker, R.L., 1995. Bounded variable least squares: an algorithm and applications. *Comput. Stat.* 10, 129–141.
- Stein, S., Wysession, M., 2003. *An Introduction to Seismology, Earthquakes, and Earth*

- Structure, 1st ed. Blackwell Publishingpp. 269–270 chapter 4.6.3.
- Tapponnier, P., Molnar, P., 1977. Active faulting and tectonics in China. *J. Geophys. Res.* 82, 2905–2930.
- Tapponnier, P., Xu, Z., Roger, F., et al., 2001. Oblique stepwise rise and growth of the Tibet Plateau. *Science* 294, 1671–1677.
- Taylor, M., Yin, A., 2009. Active structures of the Himalayan-Tibetan orogen and their relationships to earthquake distribution, contemporary strain field, and Cenozoic volcanism. *Geosphere* 5, 199–214.
- Waldhauser, F., Ellsworth, W.L., 2000. A double-difference earthquake location algorithm: method and application to the northern Hayward fault. *Bull. Seismol. Soc. Am.* 90, 1353–1368.
- Wang, H., Elliott, J.R., Craig, T.J., Wright, T.J., Liu-Zeng, J., Hooper, A., 2014. Normal faulting sequence in the Pumqu-Xainza Rift constrained by InSAR and teleseismic body-wave seismology. *Geochem. Geophys. Geosyst.* 15, 2947–2963.
- Wang, H., Ge, L., Xu, C., Du, Z., 2007. 3-D coseismic displacement field of the 2005 Kashmir earthquake inferred from satellite radar imagery. *Earth Planets Space* 59, 343–349.
- Wells, D.L., Coppersmith, K.J., 1994. New empirical relationships among magnitude, rupture length, rupture width, rupture area and surface displacement. *Bull. Seismol. Soc. Am.* 84, 974–1002.
- Wesnousky, S.G., 2006. Predicting the endpoints of earthquake ruptures. *Nature* 444, 358–360.
- Wright, T., Parsons, B.E., Jackson, J.A., et al., 1999. Source parameters of the 1 October 1995 Dinar (Turkey) earthquake from SAR interferometry and seismic bodywave modelling. *Earth Planet. Sci. Lett.* 172, 23–37.
- Wright, T.J., Elliott, J.R., Wang, H., Ryder, I., 2013. Earthquake cycle deformation and the moho: implications for the rheology of continental lithosphere. *Tectonophysics* 609, 504–523.
- Yule, D., Sieh, K., 2003. Complexities of the San Andreas fault near San Geronio Pass: implications for large earthquakes. *J. Geophys. Res.* 108, 2548. <http://dx.doi.org/10.1029/2001JB000451>.
- Zan, F.D., Gurarnieri, A.M.M., 2006. TOPSAR, terrain observation by progressive scans. *IEEE Trans. Geosci. Remote Sens.* 44, 2352–2360.
- Zhang, P., Molnar, P., Burchfiel, B.C., Royden, L., Wang, Yipeng, Deng, Qidong, Song, Fangmin, Zhang, Weiqi, Jiao, Decheng, 1988. Bounds on the Holocene slip rate of the Haiyuan fault, North-Central China. *Quat. Res.* 30, 151–164.
- Zhang, P.Z., Shen, Z., Wang, M., et al., 2004. Continuous deformation of the Tibet Plateau from global positioning system data. *Geology* 32, 809–812.